Enhanced magnetochiral effects at microwave frequencies by a single metamolecule

Satoshi Tomita,[1,*] Hiroyuki Kurosawa,[2,3] Kei Sawada,[4] and Tetsuya Ueda[5]

[1]*Graduate School of Materials Science, Nara Institute of Science and Technology (NAIST), 8916-5 Takayama, Ikoma, Nara 630-0192, Japan*

[2]*National Institute for Materials Science (NIMS), 1-1 Namiki, Tsukuba, Ibaraki 305-0044, Japan*

[3]*Research Institute for Electronic Science (RIES), Hokkaido University, N20W10, Sapporo, Hokkaido 001-0021, Japan*

[4]*RIKEN SPring-8 Center, 1-1-1 Kouto, Sayo, Hyogo 679-5148, Japan*

[5]*Department of Electrical Engineering and Electronics, Kyoto Institute of Technology, Matsugasaki, Sakyo, Kyoto 606-8585, Japan*

(Received 15 June 2016; revised manuscript received 13 December 2016; published 2 February 2017)

We have experimentally and numerically studied the directional birefringence of X-band microwaves by magnetochiral (MCh) effects of a single metamolecule under dc magnetic fields at room temperature. Phase and amplitude transmission coefficients from top and bottom, i.e., S parameters of S_{21} and S_{12}, are measured for the single metamolecule consisting of a copper chiral structure and ferrite cylinder in a waveguide. By applying a dc magnetic field, we observe a difference between S_{21} and S_{12}, which is an emergence of the MCh effects with simultaneous space-inversion and time-reversal symmetry breaking. Numerical calculation based on a finite element method reproduces well the experimental results of the MCh effects. The MCh effect can be enhanced by using the magnetic resonance of the ferrite cylinder. Notably, numerical calculation predicts that the MCh effect is extremely enhanced by interacting magnetic resonance with a specific resonant structural optical activity, leading to a giant MCh effect. The giant MCh effect observed in the present study originates from the one-way transparency caused by the Fano resonance in the metamolecule.

DOI: 10.1103/PhysRevB.95.085402

I. INTRODUCTION

Symmetry breaking is a fundamental interest in physics [1–3]. In condensed matter, symmetry breaking causes intriguing electromagnetic properties [4]. The break in space-inversion symmetry in chiral structures such as sugars, amino acids, and proteins, causes reciprocal structural (natural) optical activity. Broken time-reversal symmetry in magnetized materials leads to nonreciprocal magneto-optical (MO) activity; that is to say, MO effects. These optical activities look similar, but have different physical origins. The MO activity is caused by the Lorentz force on electrons, whereas the structural optical activity is due to electromagnetic induction in the chiral structures.

It is natural and interesting to ask what electromagnetic waves will experience when time-reversal and space-inversion symmetries are simultaneously broken. A combination of MO and structural optical activities, gives rise to the directional birefringence independent of polarizations; that is, *magnetochiral (MCh) effects* [5–8]. The MCh effect is promising for new functional devices such as a polarization-independent nonreciprocal "one-way mirror." Moreover, the quest for large MCh effects paves a way toward the realization of a synthesized gauge field; for example, an effective magnetic field for electromagnetic waves [9,10]. The system with the symmetries broken simultaneously is of interest also in terms of topological spin textures like skyrmion [11]. The MCh effect at room temperature is, however, much weaker than MO and structural optical activities in natural materials [8,12–19]. A similar phenomenon called the optical magnetoelectric (ME) effect is observed in multiferroic materials [20–23]. Intensive research efforts have been devoted to enhancing the optical ME effect by using photonic crystals [24], gratings [25], and multilayers [26] mainly in optical regions. In this way, the MCh effects can be enhanced by artificial structures [27]; for example, metamaterials [28–31].

In a previous study [32], we reported the direct observation of MCh effects in the X-band microwave region by a single metamolecule consisting of a ferrite rod and a metallic chiral structure at room temperature. A weak dc magnetic field of 1 mT was found to induce the MCh effects at frequencies of resonant structural optical activities, referred to as chiral resonances. The MCh effects were increased as the dc magnetic field was increased up to $\pm$200 mT. The difference in nonreciprocal refractive index due to the MCh effect was in the order of 10^{-3}, which was much larger than that observed in natural materials at the visible frequencies [14]. The large MCh effect is associated with the chiral resonance in the metallic chiral structure. However, the interaction of the chiral resonance with the magnetic resonance by the ferrite rod remained to be addressed. By applying strong magnetic fields, the magnetic resonance of the ferrite rod approaches the chiral resonance frequencies. This motivates a further enhancement of MCh effects.

Here we report a comprehensive study of enhanced MCh effects at microwave frequencies by a single metamolecule. Microwave transmission coefficients, S parameters of S_{21} and S_{12}, are measured through the single metamolecule under magnetic fields up to $\pm$400 mT. We observe the difference between S_{21} and S_{12} in amplitude and phase, which is reproduced by numerical calculation based on a finite element method. The difference is caused by the MCh effect with simultaneous space-inversion and time-reversal symmetry breaking. We demonstrate that the MCh effect can be enhanced by using the ferrite meta-atom magnetic resonance. Moreover, numerical calculation reveals an enormous enhancement of the MCh effect by interacting the magnetic resonance with a specific chiral resonance, leading to the giant MCh effect. The enhancement mechanisms are revealed by investigating

*tomita@ms.naist.jp

the electromagnetic field distributions in the metamolecule. The present study paves a way toward the realization of a synthesized gauge field for electromagnetic waves [9,10], and is one further step for *meta-condensed-matter physics* using metamaterials.

This paper is organized as follows. Section II shows the experimental procedures and results of X-band microwave transmission measurements through a single MCh metamolecule in a waveguide under strong magnetic fields. In Sec. III, numerical calculations reproduce the experimental results and shed light on the physics of the MCh effects. Sec. IV outlines and discusses the mechanism of the enhanced and giant MCh effects by the metamolecules, and Sec. V concludes the paper.

II. EXPERIMENT

A. Sample preparation and measurements

An MCh metamolecule has been implemented by using a Cu chiral structure (chiral meta-atom) and yttrium iron garnet (YIG) ferrite cylinder (magnetic meta-atom). Figure 1(a) shows a photograph of an MCh metamolecule in this study. A Cu wire 0.55 mm in diameter was coiled clockwise four times around the thread groove of the right-handed screw to form the right-handed Cu chiral meta-atom, as illustrated in the left part of Fig. 1(a). As shown in the right-hand side in Fig. 1(a), the diameter and length of the YIG ferrite magnetic meta-atom were 2 and 15 mm, respectively. The ferrite cylinder is well insulating. The magnetic meta-atom was inserted in the chiral meta-atom and the metamolecule was fixed in a thermal-contraction tube.

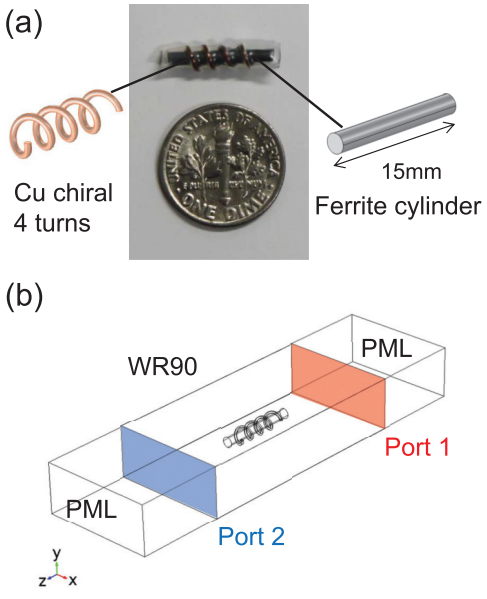

FIG. 1. (a) Photograph of MCh metamolecule (center). The diameter of the coin in the photo is 17.91 mm. Illustrations of Cu chiral meta-atom (left) and ferrite magnetic meta-atom (right). (b) Setup for numerical calculation. A metamolecule is put in the center of the WR-90 waveguide. Both sides of the waveguide are terminated with perfectly matched layers (PMLs).

A single metamolecule was put into a WR-90 waveguide, which was terminated at both ends by Agilent 281A adaptors. Because ac magnetic fields of microwaves in the waveguide are parallel to the chiral axis of the MCh metamolecule, chiral resonance can be excited. Two adaptors were connected via the waveguide so that the polarization plane of an electric field of the fundamental TE_{10} mode in an adaptor was parallel to that in the other adaptor. The sample in the waveguide was placed between two poles in an electromagnet for applying dc magnetic fields. The dc magnetic field $\mu_0 H_{\rm ext}$ was monitored by using a gauss meter equipped with a Hall element. $\mu_0 H_{\rm ext} > 0$ ($\mu_0 H_{\rm ext} < 0$) corresponds to magnetic field direction from port 1 to port 2 (port 2 to port 1). The magnetic meta-atom shows a soft magnetic nature so that the magnetization is saturated by applying dc magnetic fields of approximately 50 mT. An X-band microwave source was an Agilent PNA N5224 vector network analyzer. We measured S parameters of S_{21} and S_{12} corresponding, respectively, to transmission coefficients from port 1 to port 2 and from port 2 to port 1, simultaneously. All measurements were carried out at room temperature.

B. Experimental results

Figures 2(a)–2(d) illustrate transmission amplitude spectra for S_{21} (red curves) and S_{12} (blue curves) of the metamolecule at various magnetic fields. Figures 2(e)–2(h) are corresponding phase spectra. The microwaves above 7 GHz transmit, whereas the microwaves below 7 GHz attenuate, which is the cut-off frequency of the WR-90 waveguide. In Fig. 2(a), when $\mu_0 H_{\rm ext} = 0$ mT, we observe salient dips at 9.1, 12.2, and 13.4 GHz, which are respectively labeled A, B, and D. An additional small dip is observed at 12.6 GHz as labeled C. The dips are traced back to chiral resonances [33,34], which are enhanced optical activities due to the resonance of the chiral structures. The mode characters of the chiral resonances are explored in more detail using numerical calculation in Sec. III. The chiral meta-atom rotates the polarization plane of the electric field of microwaves and the microwaves do not transmit due to the parallel configuration of the adaptors at the end of the waveguide.

The inset shows enlarged spectra for S_{21} (red) and S_{12} (blue) at the chiral resonance A. When $\mu_0 H_{\rm ext} = 0$ mT, S_{21} and S_{12} spectra are identical at the chiral resonance frequency. Phase spectra exhibit dispersion-type signals at the chiral resonances A, B, and D when $\mu_0 H_{\rm ext} = 0$ mT although they are too weak to be observed in Fig. 2(e). The inset corresponds to the enlarged phase spectra for S_{21} (red) and S_{12} (blue) around 9.1 GHz. S_{21} and S_{12} phase spectra are identical when $\mu_0 H_{\rm ext} = 0$ mT as well as amplitude spectra. The signals demonstrate a dispersion-type shape in the phase spectra due to the Kramers-Kronig relation.

When applying $\mu_0 H_{\rm ext}$ of +201 mT [Fig. 2(b)], an appearance of another large dip is seen at 8.5 GHz, which is labeled E. The dispersion-type signal is exhibited in corresponding phase spectra [Fig. 2(f)]. The signals are shifted to higher frequencies as $\mu_0 H_{\rm ext}$ is increased. In this way, an origin of the signal E is magnetic resonance, which corresponds to precession of electron spins in the ferrite magnetic meta-atom. In Fig. 2(b), S_{21} (red) and S_{12} (blue) highlight a difference

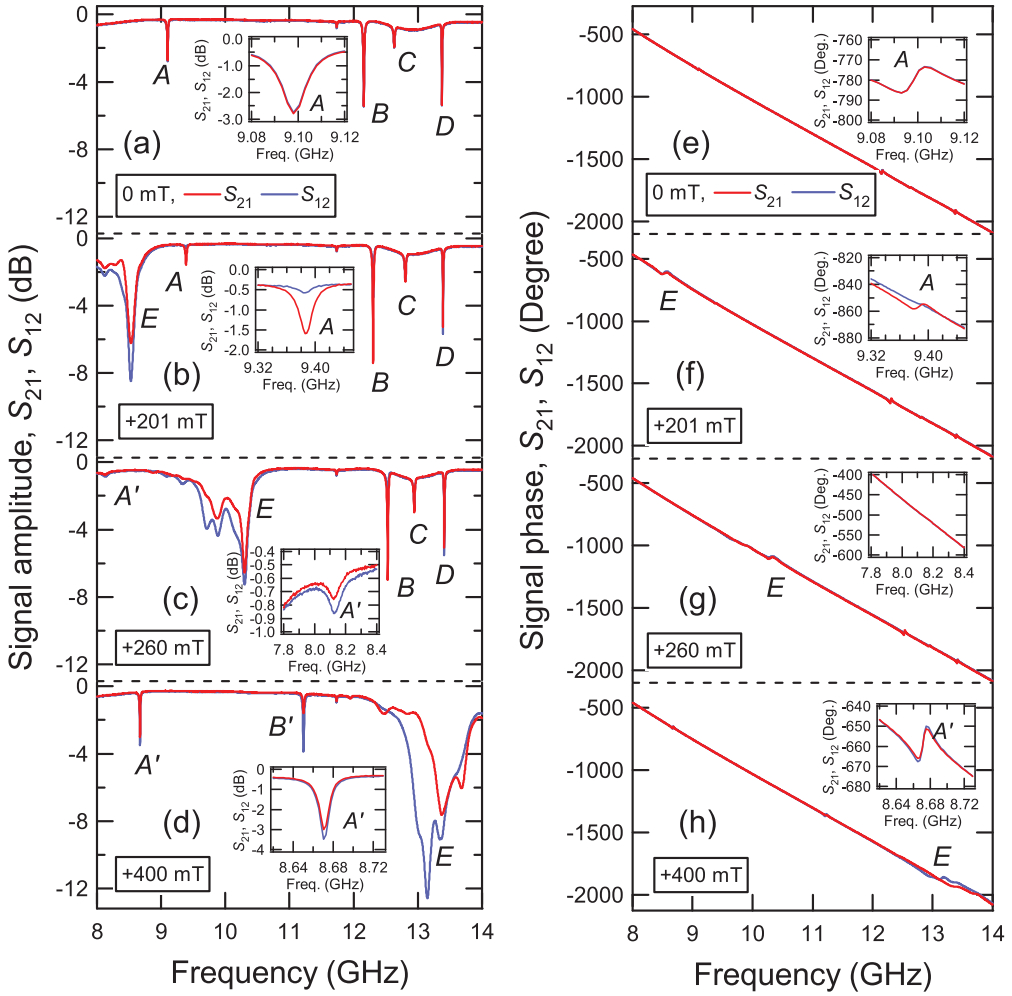

FIG. 2. Transmission S_{21} (red curves) and S_{12} (blue curves) amplitude spectra [(a)–(d)] and phase spectra [(e)–(h)] of a single MCh metamolecule under external dc magnetic fields of 0 mT [(a) and (e)], +201 mT [(b) and (f)], +260 mT [(c) and (g)], and +400 mT [(d) and (h)]. Chiral resonances are labeled A, B, C, and D, while magnetic resonance is labeled E. Insets illustrate enlarged spectra for S_{21} (red) and S_{12} (blue) of chiral resonance originally appearing at 9.1 GHz.

at the magnetic resonance E; the blue dip is much deeper than the red one. The difference represents nonreciprocity in microwave transmission.

The appearance of the magnetic resonance E is accompanied by slight shifts of the chiral resonances. Moreover, as shown in the insets in Figs. 2(b) and 2(f), S_{21} and S_{12} spectra at the chiral resonance A are not identical. In Fig. 2(b), the dips in S_{21} (red) at signals A are deeper than those in S_{12} (blue). We recall here that the magnetic resonance E is located at 8.5 GHz when $\mu_0 H_{\text{ext}} = +201$ mT. Nevertheless, nonreciprocity with a finite difference between S_{21} and S_{12} spectra is observed at the chiral resonances.

When $\mu_0 H_{\text{ext}}$ is increased up to +260 mT as shown in Figs. 2(c) and 2(g), the frequency of the magnetic resonance E shifts to approximately 10 GHz and overtakes the chiral resonance A originally at 9.1 GHz. The nonreciprocity at the magnetic resonance E becomes larger. Notably in the inset of Fig. 2(c), the chiral resonance appears at a lower frequency approximately 8.1 GHz, which is labeled A', after being passed by the magnetic resonance E. Interestingly, as demonstrated in the inset, the nonreciprocity at the chiral resonance A' flips the sign; the dip in S_{12} (blue) is deeper than that of S_{21} (red) for signal A', while the dip in S_{12} is shallower than that of S_{12} for the signal A. These results indicate that the chiral resonance A jumps to A' at a lower frequency and the sign of the nonreciprocity at the chiral resonance is inverted after being passed by the magnetic resonance E.

As $\mu_0 H_{\text{ext}}$ is increased up to +400 mT as shown in Figs. 2(d) and 2(h), the magnetic resonance E shifts to 13 GHz and demonstrates very large nonreciprocity. After overtaking by the magnetic resonance, the chiral resonance B originally at 12.2 GHz is shifted to a lower frequency of 11.2 GHz, which is labeled B'. The dip in S_{12} is deeper than that in S_{21} at the signal B'. The chiral resonance A' at a lower frequency shifts to a higher frequency of 8.7 GHz, which is close to the initial frequency of the signal A.

Figure 3 demonstrates the differences between S_{21} and S_{12}, i.e., nonreciprocity signals in amplitudes at various magnetic fields from 0 to ±400 mT. Figure 4 shows the corresponding phase difference spectra. A featureless spectrum is obtained with $\mu_0 H_{\text{ext}} = 0$ mT (a black line). The upper halves of Figs. 3 and 4 highlight signals due to nonreciprocity with $\mu_0 H_{\text{ext}} > 0$.

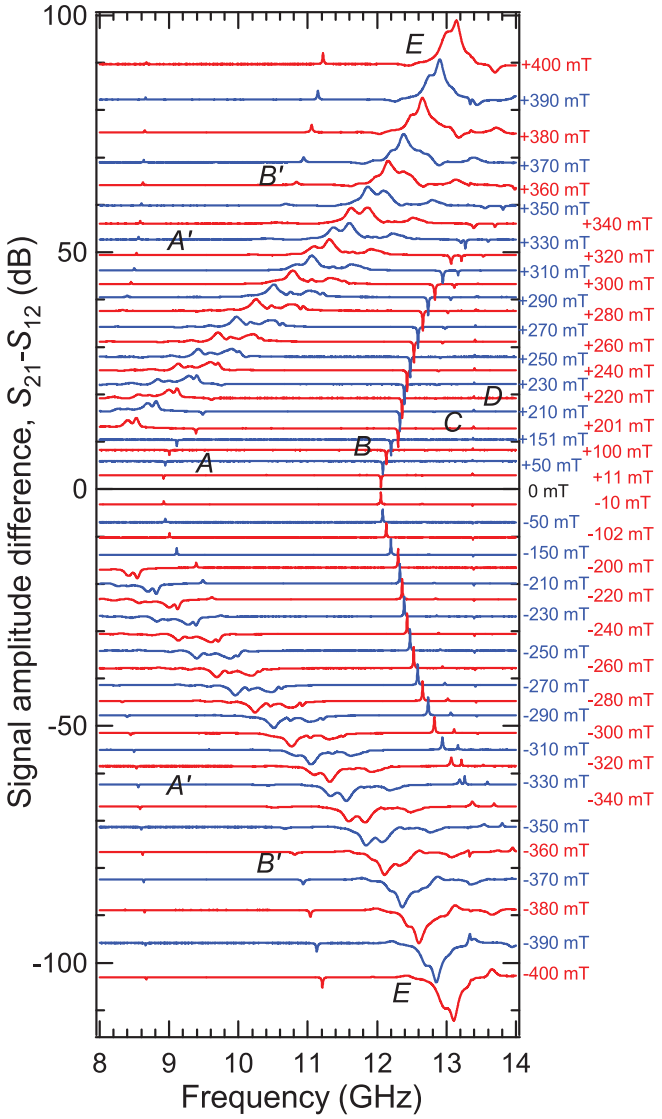

FIG. 3. Differences in amplitudes between S_{21} and S_{12} from 8 to 14 GHz of an MCh metamolecule under dc magnetic fields from 0 to ±400 mT.

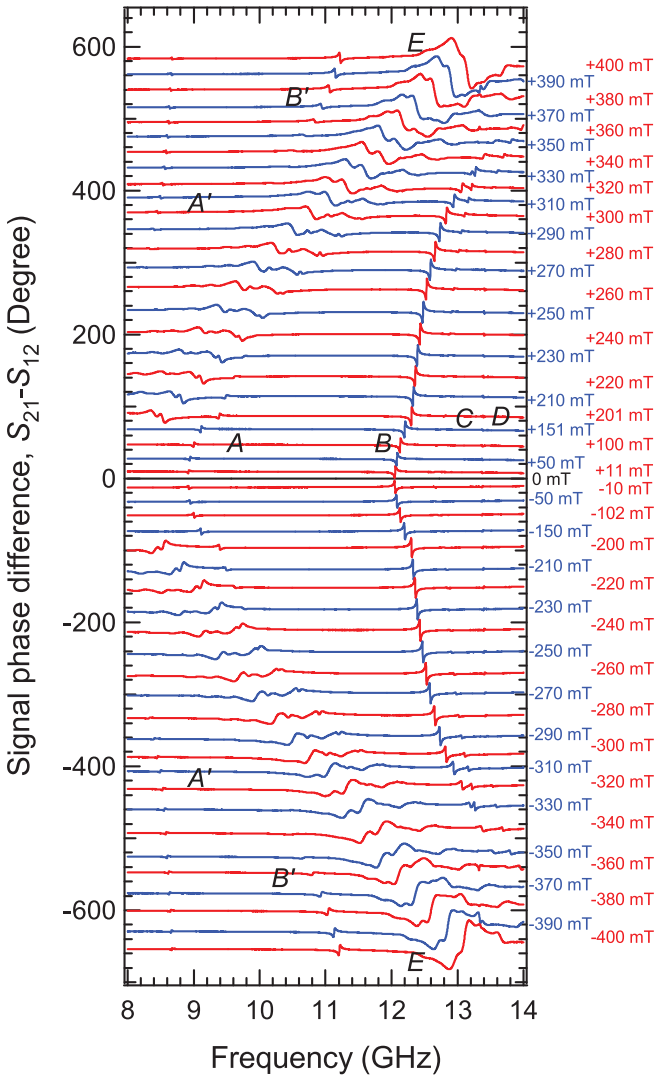

FIG. 4. Differences in phases between S_{21} and S_{12} from 8 to 14 GHz of an MCh metamolecule under dc magnetic fields from 0 to ±400 mT.

When $\mu_0 H_{\rm ext} = +11$ mT in Fig. 3, a weak dip due to the chiral resonance A emerged at 8.9 GHz. A dispersion-type signal is observed at the same frequency in Fig. 4. An increase in $\mu_0 H_{\rm ext}$ leads to a blueshift and enhancement of the nonreciprocity signals at the chiral resonances A, B, and C.

When $\mu_0 H_{\rm ext} = +201$ mT, nonreciprocity signals associated with the magnetic resonance E appear at approximately 8.5 GHz in Figs. 3 and 4. The nonreciprocity signal due to the magnetic resonance shifts to higher frequencies and becomes larger as $\mu_0 H_{\rm ext}$ is increased. Under $\mu_0 H_{\rm ext} = +250$ mT, the magnetic resonance E is overlapped with the chiral resonance A, resulting in a disappearance in the chiral resonance A. At $\mu_0 H_{\rm ext} = +280$ mT, a peak labeled A' is observed at approximately 8.3 GHz, a slightly lower frequency below 9 GHz. The sign of the nonreciprocity signal due to the chiral resonance is inverted. The nonreciprocity signal due to the chiral resonance B shows a very similar behavior to that due to the chiral resonance A. The nonreciprocity signals due to the magnetic resonance in Figs. 3 and 4 become significantly large at +400 mT. The maximum values of amplitude and phase differences were respectively 9.11 dB and 20.8° by the magnetic resonance at approximately 13 GHz under +400 mT.

Differential spectra for the reversed direction of the external dc magnetic field ($\mu_0 H_{\rm ext} < 0$) are also illustrated in the lower halves of Figs. 3 and 4. While the appearance and frequency shift of nonreciprocity signals are very similar to those in $\mu_0 H_{\rm ext} > 0$, the sign is flipped with the direction of the magnetic field. Figures 3 and 4 demonstrate that the nonreciprocity signals at the magnetic resonance E and chiral resonances A, B are odd with respect to $\mu_0 H_{\rm ext}$.

In the following section, we carry out a numerical simulation to reproduce the experimental results. Nonreciprocity signals at a much higher magnetic field are addressed. Moreover, the chirality dependence of the nonreciprocity signals is studied numerically. We gain insight into the underlying physics by visualizing the electromagnetic responses in the metamolecule.

III. NUMERICAL CALCULATION

A. Calculation setup

A numerical calculation based on a finite element method is performed using COMSOL MULTIPHYSICS. Figure 1(b) illustrates the calculation configuration. The metamolecule is placed in the center of a WR-90 waveguide. The WR-90 waveguide is filled with air. The structural parameters of the metamolecule and the waveguide are identical to those in the experiments. The surfaces of the chiral meta-atom and the waveguide are modeled as perfect electric conductors. Both sides of the waveguide are terminated with perfectly matched layers (PMLs). S_{21} and S_{12} of microwaves with TE_{10} mode are calculated.

The material parameters for the ferrite cylinder are modeled as follows. The dielectric constant of the ferrite is set to $14.5 + 0.0029i$. When an external dc magnetic field is applied in the $+z$ direction, the ferrite with the anisotropic magnetic permeability is magnetized in the $+z$ direction as

$$\hat{\mu} = \begin{pmatrix} \mu & -i\kappa & 0 \\ i\kappa & \mu & 0 \\ 0 & 0 & \mu_0 \end{pmatrix}, \tag{1}$$

where

$$\kappa = i\mu_0\chi_{xy}, \tag{2}$$

$$\mu = \mu_0(1 + \chi_{xx}). \tag{3}$$

On the off-diagonal component, κ is proportional to the external magnetic field and gives the MO activities such as the Faraday effect.

The magnetic susceptibility tensor χ is given by

$$\chi_{xx} = \frac{\omega_0\omega_m\left(\omega_0^2 - \omega^2\right) + \omega_0\omega_m\omega^2\alpha^2}{\left[\omega_0^2 - \omega^2(1+\alpha^2)\right]^2 + 4\omega_0^2\omega^2\alpha^2} + i\frac{\alpha\omega\omega_m\left[\omega_0^2 + \omega^2(1+\alpha^2)\right]}{\left[\omega_0^2 - \omega^2(1+\alpha^2)\right]^2 + 4\omega_0^2\omega^2\alpha^2}, \tag{4}$$

$$\chi_{xy} = \frac{2\omega_0\omega_m\omega^2\alpha}{\left[\omega_0^2 - \omega^2(1+\alpha^2)\right]^2 + 4\omega_0^2\omega^2\alpha^2} - i\frac{\omega\omega_m\left[\omega_0^2 - \omega^2(1+\alpha^2)\right]}{\left[\omega_0^2 - \omega^2(1+\alpha^2)\right]^2 + 4\omega_0^2\omega^2\alpha^2}, \tag{5}$$

where $\omega_0 = \gamma\mu_0 H_{\text{ext}}$, $\omega_m = \gamma\mu_0 M_s$, and $\alpha = \gamma\mu_0\Delta H/(2\omega)$. Here, ω_0 is the Larmor frequency at $\mu_0 H_{\text{ext}}$. ω_m is the Larmor frequency at the saturation magnetization M_s. α is the loss factor, or the Gilbert damping factor, of the ferrite, and ΔH is the corresponding linewidth. γ is the gyromagnetic ratio of the electron. Note that the material parameters of the ferrite cylinder used in our numerical calculation are not the same as those in the experiment; we used the specific parameters for the ferrite from the literature [35]. The difference in the parameters between the experiment and the numerical calculation influences the resonance frequencies. However, it does not affect the physics behind the phenomena.

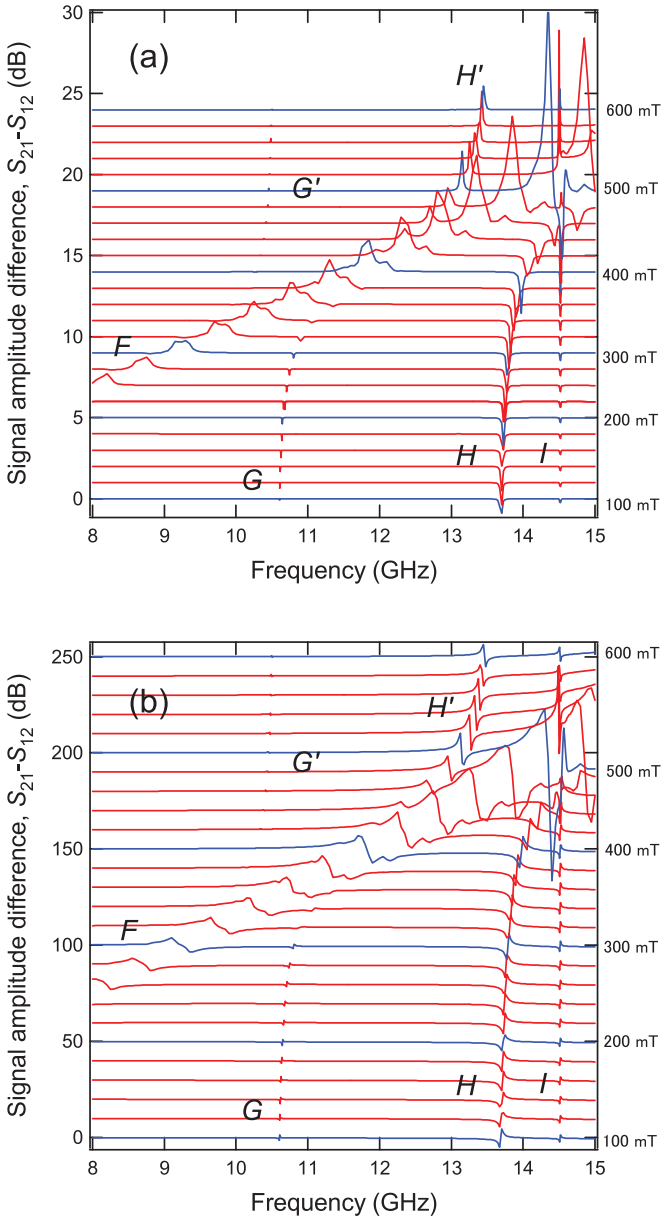

FIG. 5. Differences in calculated (a) amplitudes and (b) phases spectra between S_{21} and S_{12} between 8 and 15 GHz for an MCh metamolecule under dc magnetic fields from +100 to +600 mT. Magnetic resonance is labeled F, while chiral resonances are labeled G, H, and I.

B. Numerical results

Figure 5(a) illustrates the calculated differential spectra in amplitudes between S_{21} and S_{12} of the MCh metamolecule under dc magnetic fields. Figure 5(b) shows the corresponding phase spectra. The external magnetic field $\mu_0 H_{\text{ext}}$ was varied from +100 to +600 mT with steps of 20 mT. The chirality of the chiral meta-atom is set to be right-handed, which is same as the experiments. The spectra in Figs. 5(a) and 5(b) highlight three features. The first is a nonreciprocity signal

labeled F with broad linewidth, for example, at approximately 9 GHz with $\mu_0 H_{\text{ext}} = +300$ mT. This signal shifts to a higher frequency and becomes larger as $\mu_0 H_{\text{ext}}$ is increased. This signal is thus caused by the magnetic resonance of the ferrite magnetic meta-atom in the metamolecule.

The second feature is nonreciprocity signals with narrow linewidth at approximately 10.6 and 13.7 GHz (labeled G and H) when $\mu_0 H_{\text{ext}} = +100$ mT. These signals are associated with the chiral resonance in the metamolecule. The resonances G and H in the numerical results correspond to those A and B in the experimental results. As $\mu_0 H_{\text{ext}}$ is increased and the magnetic resonance F of the ferrite magnetic meta-atom approaches, the signals G and H slightly shift to higher frequencies. The nonreciprocity signals G and H flip the sign after being passed by the magnetic resonance F. These features are very similar to those observed in the experiment (Figs. 3 and 4).

The last feature is a nonreciprocity signal labeled I with narrow linewidth at approximately 14.5 GHz in Fig. 5. This signal is associated with the chiral resonance. The behavior of the signal is, however, quite different from those of other chiral resonances G and H at lower frequencies. The signal I does not shift to a higher frequency as $\mu_0 H_{\text{ext}}$ is increased. More importantly, the nonreciprocity signal I is strongly enhanced as the magnetic resonance approaches under $\mu_0 H_{\text{ext}} = +500$ mT.

The sign of the nonreciprocity signals in the numerical calculation flipped by changing the dc magnetic field direction, although not shown here. Furthermore, neither only chiral meta-atom nor magnetic meta-atom exhibited nonreciprocity signals in the numerical calculation. We also confirmed in the numerical calculation that $\hat{\mu}$ without the off-diagonal parts (i.e., $\kappa = 0$) of the metamolecule resulted in the reciprocity signals.

In order to investigate the strong enhancement of the chiral resonance I in more detail, calculation was carried out with varying $\mu_0 H_{\text{ext}}$ in the vicinity of +500 mT. Figure 6(a) illustrates the calculated amplitude difference of S_{21} and S_{12} as $\mu_0 H_{\text{ext}}$ is varied from +495 to +510 mT with steps of 5 mT. Figure 6(b) shows the corresponding phase spectra. The nonreciprocity signal I is extremely enhanced with $\mu_0 H_{\text{ext}}$ of +505 mT. Additionally, in Fig. 6(a), the symmetric dispersive structure of signal I under 495 mT becomes the asymmetric peak structure under +505 mT. Figures 6(a) and 6(b) demonstrate that, when $\mu_0 H_{\text{ext}} = +505$ mT, the amplitude and phase differences around 14.446 GHz are evaluated to be 48.26 dB and 166.8°, respectively.

Figure 7 illustrates the pseudocolor plot for the calculated differences in phase spectra between S_{21} and S_{12}. The vertical axis corresponds to the frequency in the range from 8 to 15 GHz. The horizontal axis corresponds to $\mu_0 H_{\text{ext}}$ from +100 to +600 mT. In Fig. 7, the pseudocolor plot of $\log[|\arg(S_{21} - S_{12})|]$ is shown in order to make weak chiral resonances more visible. Three chiral resonances G, H, and I are observed, together with the magnetic resonance F, of which the frequency depends linearly on $\mu_0 H_{\text{ext}}$. The pseudocolor plot demonstrates that the chiral resonances G and H have anticrossing features in the vicinity of the magnetic resonance of the ferrite magnetic meta-atom [36].

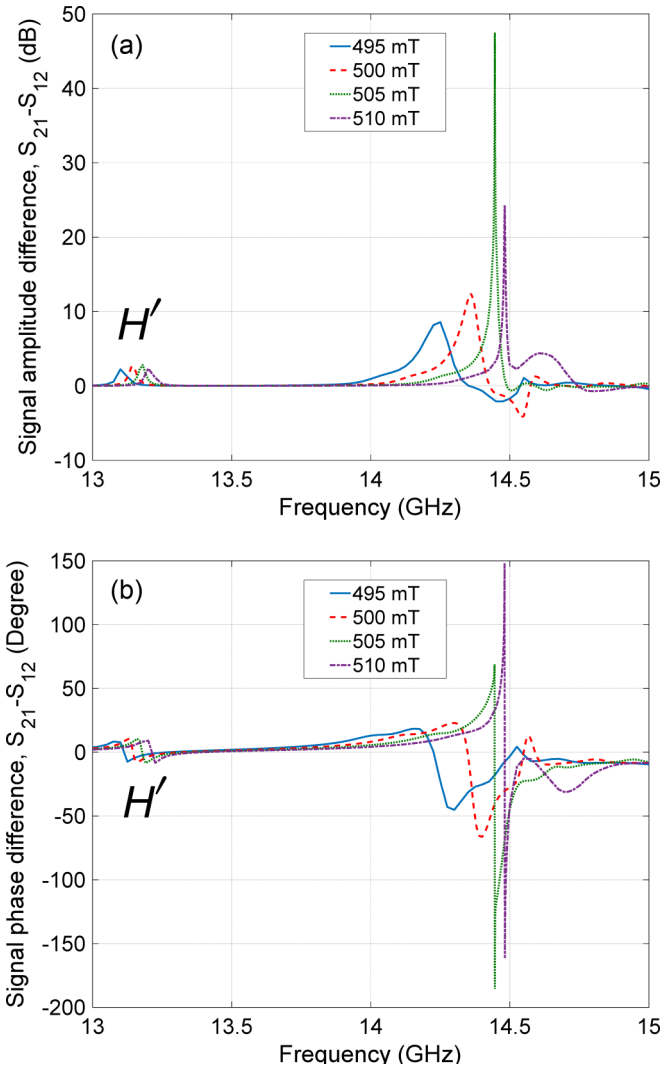

FIG. 6. Calculated differential spectra between S_{12} and S_{21} of amplitude (a) and phase (b) in the vicinity of $\mu_0 H_{\text{ext}} = +500$ mT. $\mu_0 H_{\text{ext}}$ is varied from 495 to 510 mT with steps of 5 mT.

The anticrossing nature of the chiral resonances G and H is caused by the hybridization with the magnetic resonances F. Contrastingly, Fig. 7 highlights that the chiral resonance I is independent of $\mu_0 H_{\text{ext}}$ and does not show an anticrossing feature.

The chirality dependence of the nonreciprocity signals is investigated numerically since it is difficult to prepare identical chiral meta-atoms reproducibly and precisely in experiments as in our previous report [32]. In the calculation, the metamolecule chirality was switched by changing the chirality of the chiral meta-atom. Figure 8(a) illustrates the amplitude difference spectra between S_{21} and S_{12} of the right-handed metamolecule, while Fig. 8(b) illustrates those of the left-handed metamolecule. In these figures, $\mu_0 H_{\text{ext}}$ is increased from +100 to +600 mT with steps of 50 mT. Figures 8(a) and 8(b) demonstrate that the sign of the nonreciprocity response at the chiral resonance frequency of 10.6 GHz flips its sign depending on the meta-atom's chirality. Furthermore, the nonreciprocity signal sign associated with the magnetic

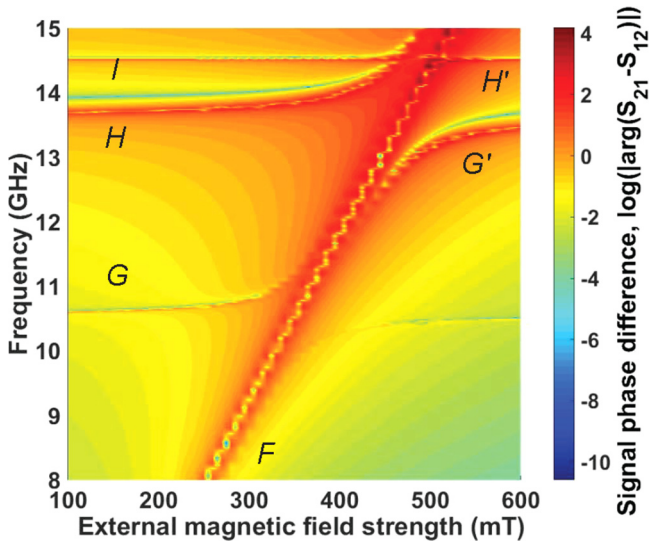

FIG. 7. Pseudocolor plot for differences in calculated phase between S_{21} and S_{12} in the range from 8 to 15 GHz. External dc magnetic fields vary from +100 to +600 mT.

resonance (e.g., at 10.5 GHz under $\mu_0 H_{\text{ext}} = +350$ mT) also depends on the chirality. The sign of the phase differential spectra also flips depending on the chirality of the chiral meta-atom (not shown).

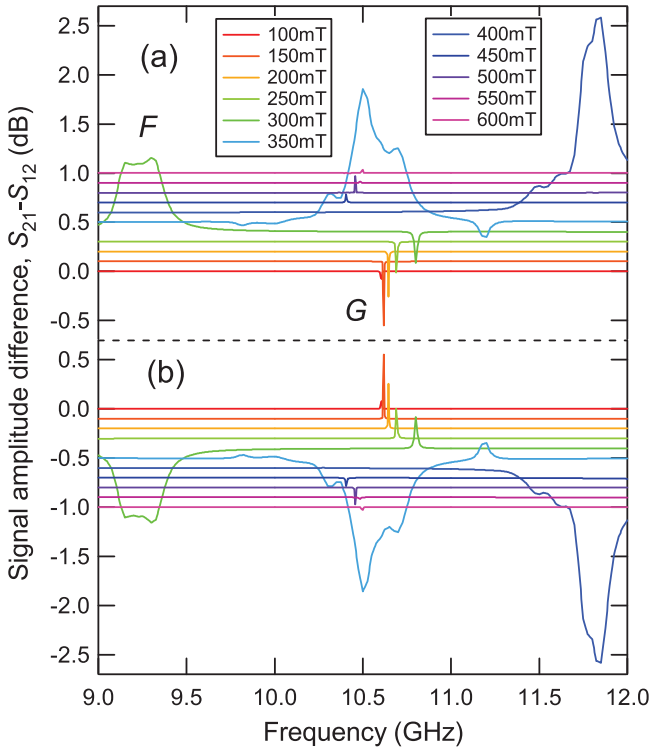

FIG. 8. Differences in calculated amplitude spectra between S_{21} and S_{12} between 9 and 12 GHz of (a) right- and (b) left-handed MCh metamolecules. External dc magnetic field varies from +100 to +600 mT with steps of 50 mT.

IV. DISCUSSION

A. Enhanced MCh effects with chiral or magnetic resonances

The present experimental results of microwave transmission through a single metamolecule under dc magnetic fields highlight the nonreciprocity signals in the differential spectra for $S_{21} - S_{12}$ in Sec. II. The signals were observed at frequencies of the chiral resonances or magnetic resonance. The nonreciprocity signal due to the magnetic resonance shifted to higher frequency and was significantly enhanced as $\mu_0 H_{\text{ext}}$ was increased. On the other hand, the nonreciprocity signals due to the chiral resonances shifted slightly to higher frequencies as the magnetic resonance approached, and then jumped to lower frequencies flipping sign as the magnetic resonance was surpassed. By changing the direction of $\mu_0 H_{\text{ext}}$, the sign of the nonreciprocity signals associated with both chiral and magnetic resonances was flipped (Figs. 3 and 4). We have succeeded in reproducing these experimental results by numerical calculation as described in Fig. 5 in Sec. III. Moreover, numerical calculation indicated that the sign of the nonreciprocity signals was flipped by changing the chirality of the chiral meta-atom in the metamolecule (Fig. 8). These experimental and numerical studies demonstrate that the nonreciprocity signals were odd with respect to both the magnetic field and chirality. Additionally, the numerical calculation pointed out that neither chiral meta-atom nor magnetic meta-atom exhibited nonreciprocity signals. Therefore, the nonreciprocity signals observed in this study are an emergence of MCh effects because the MCh effect is represented by the cross products of MO (i.e., κ) and structural optical activities (i.e., chiral parameter ξ).

The direct observation of the MCh effects is attributed to two advantages for the metamolecule in microwave regions [32]: the chiral resonance in the chiral meta-atom [34] and the large magnetic response of the magnetic meta-atom in microwave regions. Notably, the MCh effect can be obtained by the magnetic resonance even in the absence of the chiral resonance since the space-inversion symmetry of the system is broken. The present experimental and numerical results in Figs. 3–5 highlight that the MCh effect due to the magnetic resonance is much larger than that due to chiral resonances except for the chiral resonance I in the calculation. The MCh effect due to the magnetic resonance brings about the maximum values of amplitude and phase differences as 9.11 dB and 20.8°, respectively, experimentally observed at approximately 13 GHz under $\mu_0 H_{\text{ext}} = +400$ mT.

The phase and amplitude differences in the transmission coefficients can be converted to the nonreciprocal differences in the real and imaginary parts of refractive indices $\Delta n'$ and $\Delta n''$, respectively [32]. Consider the one-dimensional structure composed of the single metamolecule inserted into a rectangular waveguide. Here, $\Delta n'$ and $\Delta n''$ between S_{21} and S_{12} of unpolarized waves are described as follows:

$$\Delta n = n_{1\to 2} - n_{2\to 1} = \Delta n' + i\,\Delta n''. \tag{6}$$

Δn is a Lorentz-type function of the operational frequency, and is related to the phase and amplitude of the complex

transmission coefficients as follows:

$$\Delta n' = -\frac{c}{2\pi f l}\Delta\phi \simeq -47.7 \times \frac{\Delta\phi}{f l}, \tag{7}$$

$$\Delta n'' = -\frac{c}{40\pi(\log_{10} e) f l}\Delta I \simeq -5.50 \times \frac{\Delta I}{f l}, \tag{8}$$

where $\Delta\phi$ denotes the phase difference $\angle S_{21} - \angle S_{12}$ in radian and ΔI the amplitude difference $|S_{21}| - |S_{12}|$ in decibel at the MCh effects. The frequency f is measured in GHz, and l represents the length of the metamolecule measured in millimeters.

In the present experiments, from Eqs. (6)–(8) with $l =$ 15 mm and $f = 13$ GHz, we evaluated $\Delta n' \simeq -8.9 \times 10^{-2}$ and $\Delta n'' \simeq -2.6 \times 10^{-1}$ maxima at $\mu_0 H_{\rm ext} = +400$ mT. $\Delta n'$ and $\Delta n''$ should satisfy the Kramers-Kronig relation, so that the magnitude of them is in the same order. Our previous study focused on the MCh effects under lower dc magnetic fields [32] reported that $\Delta n' \simeq 5.4 \times 10^{-3}$ and $\Delta n'' \simeq 1.5 \times 10^{-2}$ maxima at $\mu_0 H_{\rm ext} = +200$ mT. Thus the MCh effect enhanced by the magnetic resonance in the present experiments is one order of magnitude greater than that of the previous experiments.

B. Frequency shift and sign inversion of MCh effects

Experimental and numerical results demonstrate that the MCh signals at chiral resonance frequencies begin to shift to higher frequencies as the magnetic resonance approaches. After being passed by the magnetic resonance, the MCh signals revive at lower frequencies with an opposite sign. The shift is explained by the effective permeability in the WR-90 waveguide, which is described by $\mu \pm \kappa$. Effective permeability, except for $\mu - \kappa$, has a singularity as a function of $\mu_0 H_{\rm ext}$. As $\mu_0 H_{\rm ext}$ is increased below the singularity, the positive effective permeability increases, bringing about a shift in the chiral resonance frequency to a higher frequency. Above the singularity, the effective permeability becomes negative and increases with $\mu_0 H_{\rm ext}$, resulting in the significant redshift of the chiral resonance frequency. As $\mu_0 H_{\rm ext}$ is further increased, the chiral resonance shifts to a higher frequency and arrives at the initial chiral resonance frequency.

The sign reversal after being passed by the magnetic resonance is further evidence of the MCh effect, which is proportional to the product of the chiral parameter ξ and the off-diagonal component of the permeability κ. κ flips its sign in the vicinity of the magnetic resonance of the ferrite magnetic meta-atom. Following the sign inversion, the sign of the MCh signal is reversed. In order to elaborate the physics underlying the sign reversal, the power flow is calculated in the vicinity of the magnetic resonance of the ferrite magnetic meta-atom.

Figure 9(a) illustrates the calculated Poynting vector flow at the surface of the magnetic meta-atom under $\mu_0 H_{\rm ext} =$ $+400$ mT (chiral resonance H) as indicated by a lower arrow in the inset. The incident microwave is transmitted in the $+z$ direction (i.e., from port 1 to port 2). Since $\mu_0 H_{\rm ext}$ of $+400$ mT causes magnetic resonance F at approximately 11.8 GHz, the chiral resonance H is located at a higher frequency compared to the magnetic resonance; in other words, before being passed by the magnetic resonance. In Fig. 9(a), the Poynting vector exhibits helical flow directed to the $+z$ direction. By contrast, Fig. 9(b) illustrates the Poynting vector flow under $\mu_0 H_{\rm ext} = +500$ mT (chiral resonance H') as indicated by an upper arrow in the inset. Under $+500$ mT the magnetic resonance F shifts to approximately 14.5 GHz. This figure therefore corresponds to the case with the chiral resonance H' after being passed by the magnetic resonance. Whereas the Poynting vector flow is helical, it is directed to the $-z$ direction; that is to say, opposite to the incident direction of microwave in Fig. 9(a). These results indicate that the power flow is reversed in the vicinity of the magnetic resonance of the ferrite magnetic meta-atom. This reversal of power flow is consistent with the explanation from the viewpoint of the effective medium in the waveguide.

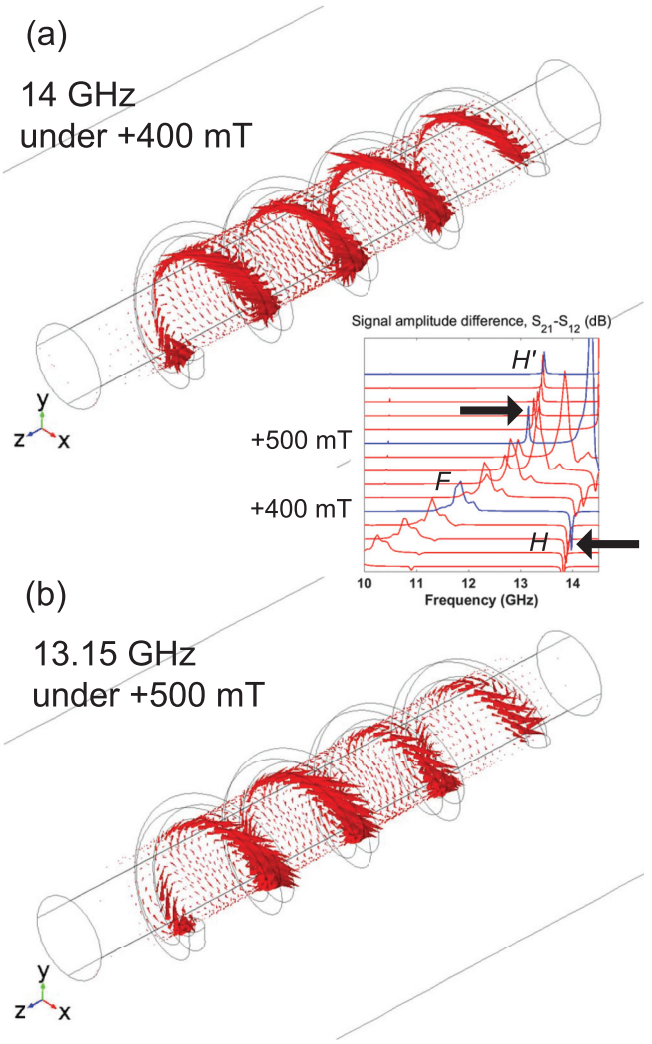

FIG. 9. Poynting vector flow in the vicinity of magnetic resonance of ferrite magnetic meta-atom at (a) 14 GHz under $+400$ mT and (b) 13.15 GHz under $+500$ mT. The length of the cone is proportional to the Poynting vector amplitude. The insets illustrate the enlarged spectra of Fig. 5(a).

C. Eigenmodes of chiral and magnetic resonances

We have numerically reproduced the spectral features of the MCh effects observed in the experiments. However,

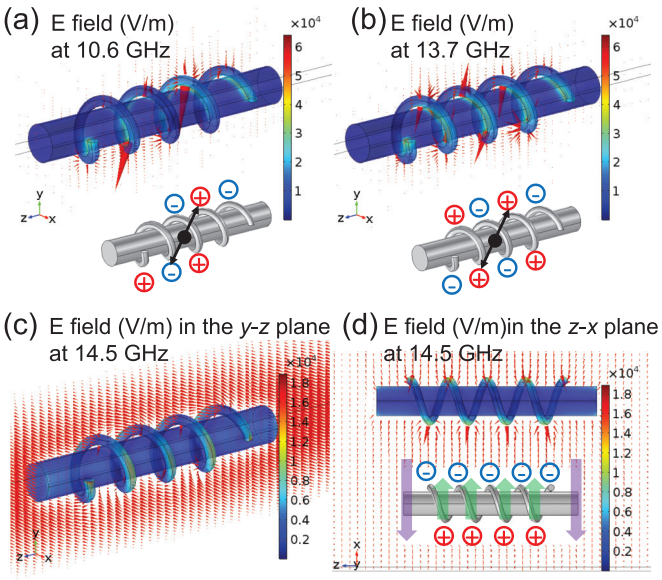

FIG. 10. Electric field distributions of three chiral resonances under +100 mT. Resonance frequencies are 10.6 (a), 13.7 (b), and 14.5 GHz [(c) and (d)], respectively. Cones and pseudocolor plots indicate electric field vectors and intensities, respectively. Vector fields in the y-z plane are illustrated in (a)–(c), whereas those in the z-x plane are illustrated in (d). Insets illustrate electric charge distributions. Purple arrows in (d) are applied electric fields on the metamolecule, while green arrows are electric fields induced by charge distribution by electric charge on the chiral meta-atom.

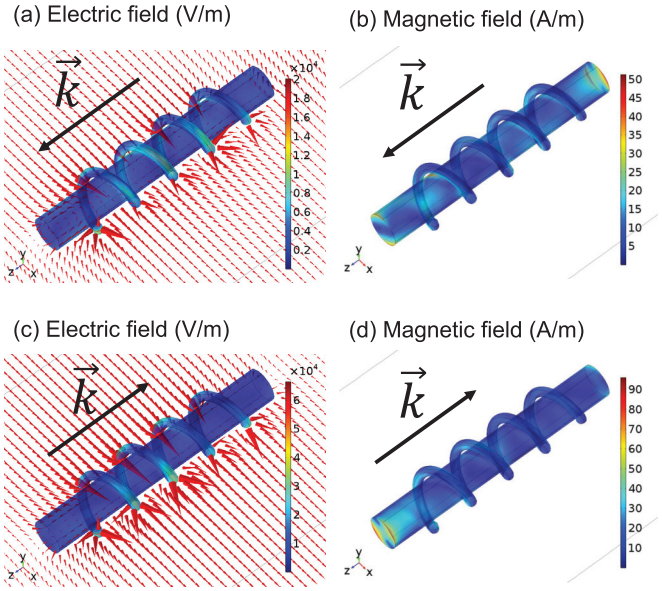

FIG. 11. Electromagnetic field distributions at 14.446 GHz under $\mu_0 H_{\text{ext}} = +505$ mT. (a), (c) Electric field vectors in the z-x plane are indicated by red cones. Pseudocolor indicates electric field intensity. (b), (d) Pseudocolor of magnetic field intensity. Incident microwaves in (a) and (b) are from port 1, whereas that in (c) and (d) is from port 2.

the eigenmodes of the chiral resonances appearing in the spectra have yet to be characterized. The eigenmodes were numerically calculated using the eigenmode solver of COMSOL MULTIPHYSICS. Figures 10(a)–10(c) illustrate electric field distributions calculated at 10.6, 13.7, and 14.5 GHz under $\mu_0 H_{\text{ext}} = +100$ mT (chiral resonances G, H, and I in Fig. 5), respectively. The cones and pseudocolor plots represent the electric field vectors and intensities, respectively.

The electric field at chiral resonance G in Fig. 10(a) exhibits spatially symmetric distribution with respect to the center of the metamolecule. By contrast, the electric field at the chiral resonance H is antisymmetric as illustrated in Fig. 10(b). This difference in the spatial symmetry is caused by the charge distributions as schematically illustrated in the insets. Under these field distributions, the chiral resonances G and H exhibit anticrossing behaviors in the vicinity of the magnetic resonance F of the ferrite meta-atom. The chiral resonance I at 14.5 GHz that does not exhibit anticrossing shows, however, completely different electric field distributions.

Figures 10(c) and 10(d) depict the electric fields at the chiral resonance I in the y-z and z-x planes, respectively. Figure 10(c) demonstrates that the electric fields are excluded from the metamolecule. The exclusion of the electric fields is more clearly seen in the field distribution in the z-x plane as highlighted in Fig. 10(d). The inset in Fig. 10(d) illustrates a schematic of the electric charge distribution pattern corresponding to the field distribution. Because the electric fields induced by the surface charge (green arrows) are antiphase to the applied electric fields (purple arrows), the electric fields in the metamolecule are canceled out. This is the reason why the electric fields are excluded from the metamolecule at the chiral resonance I. Owing to the "exclusive" nature, the chiral resonance has a weak coupling with the magnetic resonance of the ferrite magnetic meta-atom. Therefore, this chiral resonance I has no splitting features in the vicinity of the magnetic resonance F as shown in Fig. 7.

D. Giant MCh effect with both chiral and magnetic resonances

The exclusive nature of the chiral resonance does not bring about strong coupling with the magnetic resonance. On the contrary, numerical calculation demonstrates that the MCh effect was extremely enhanced by overlapping the magnetic resonance F to the exclusive chiral resonance I. Figures 6(a) and 6(b) highlight that, in calculation, the maximum values of amplitude and phase differences at the MCh effect due to the chiral resonance I around 14.446 GHz under $\mu_0 H_{\text{ext}} = +505$ mT were 48.26 dB and 166.8°, respectively. If we suppose $l = 15$ mm and $f = 14$ GHz, we evaluate $\Delta n' \simeq -6.6 \times 10^{-1}$ and $\Delta n'' \simeq -1.26$ maxima from Eqs. (7) and (8). The MCh effect predicted here in the calculation is gigantic and one order of magnitude greater than the enhanced MCh effect observed in the present experiments.

The field distributions under the MCh resonance is studied to reveal the origin of this giant MCh effect. Figure 11 illustrates the field distributions in the chiral resonance I at 14.446 GHz under +505 mT, where the amplitude difference becomes maximum. Figures 11(a) and 11(b) correspond to the incidence from port 1, whereas Figs. 11(c) and 11(d) correspond to that from port 2. In Figs. 11(a) and 11(c), the electric field distribution patterns in the z-x plane exhibit the exclusive nature found in Fig. 10(d), indicating that the chiral

meta-atom is on resonance when excited from either port. Due to the exclusive chiral resonance, the magnetic fields are also excluded from the chiral meta-atom, bringing about weak magnetic fields near the center of the metamolecule. These features are commonly observed in Fig. 11.

Contrary to the common features, two significant differences depending on the incident directions can be found in the field distribution patterns. The first is the field intensity. All the field intensities when excited from port 2 [Fig. 11(c)] are remarkably higher than those from port 1 [Fig. 11(a)], indicating that the metamolecule is on strong resonance when excited from port 2. The second is the magnetic field distributions. The magnetic field intensity when excited from port 1 [Fig. 11(b)] is high near both ends of the ferrite meta-atom, whereas that from port 2 [Fig. 11(d)] is high only near the left end of the ferrite meta-atom. This indicates large nonreciprocal transmission of microwaves. When excited from port 2, the exclusive chiral resonance is on strong resonance. The ferrite meta-atom is also on the magnetic resonance, which is enhanced by the coupling with the chiral resonance. However, due to the exclusive nature of the chiral resonance, the magnetic resonance can be strongly enhanced only near the end of the ferrite meta-atom. Under this field distribution, the incident microwave is absorbed near the left end of the ferrite meta-atom and is attenuated near the right end. The high magnetic field is thus observed only near the left end of the ferrite meta-atom.

In contrast, all the field intensities excited from port 1 are lower than those of port 2, indicating that the resonance state excited from port 1 is weak. Under the weak resonance, absorption due to the magnetic resonance is small. Thus, the incident microwave is not attenuated at the right end of the ferrite meta-atom. The combination of the weak and exclusive nature of the chiral resonance causes the weak magnetic resonance near both ends of the ferrite meta-atom. Therefore, the absorption due to the magnetic resonance shows a remarkable difference, which results in the large-amplitude difference between S_{21} and S_{12}.

E. Origin of the giant MCh effect

In Fig. 12, the calculated amplitude spectra for S_{21} and S_{12} under $\mu_0 H_{\rm ext} = +505$ mT are drawn by red and blue solid curves, respectively. A green dashed curve corresponds to the calculated amplitude spectrum for S_{21} with only magnetic meta-atom as a control. The green dashed curve has a broad dip at approximately 14.6 GHz, which is caused by the magnetic resonance of the ferrite meta-atom. In the vicinity of the magnetic resonance, there is the exclusive chiral resonance at 14.5 GHz indicated by a vertical black dashed line. The interaction between the magnetic and chiral resonance brings about the Fano-resonance feature in the amplitude spectra, which is found in the sharp dip in the S_{12} spectrum.

Here, introducing the complex amplitudes of the magnetic ($A_{\rm M}$) and chiral ($A_{\rm Ch}$) resonances, this interaction is modeled by the following equations of motion for the complex amplitudes in the steady state [37]:

$$(\delta_{\rm M} + i\gamma_{\rm M})A_{\rm M} - K A_{\rm Ch} = g_1 S_{\rm in}, \quad (9)$$

$$-K A_{\rm M} + (\delta_{\rm Ch} + i\gamma_{\rm Ch})A_{\rm Ch} = g_2 S_{\rm in}, \quad (10)$$

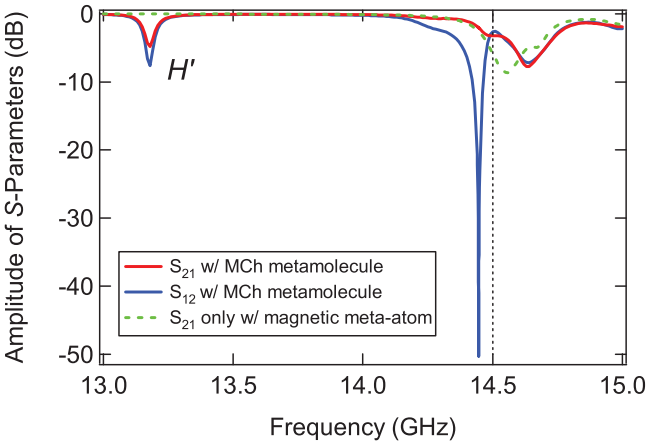

FIG. 12. Calculated amplitude spectra for S_{21} (red) and S_{12} (blue) of the MCh metamolecule between 13 and 15 GHz under $\mu_0 H_{\rm ext} = +505$ mT. The amplitude spectrum of S_{21} calculated only with magnetic meta-atom is plotted also by a green dashed curve as reference. Third chiral resonance frequency is indicated by a vertical black dashed line.

where $\delta_{\rm M}$ and $\delta_{\rm Ch}$ correspond to the frequency detunings from the magnetic and chiral resonance frequencies, respectively. $\gamma_{\rm M}$ and $\gamma_{\rm Ch}$ are respectively the damping constant of the magnetic and chiral resonances. K is the coupling parameter between the two resonance modes. g_1 and g_2 represent the coupling parameter of the magnetic and chiral resonances with the incident microwave $S_{\rm in}$, respectively.

Depending on the strength of coupling between the two resonance modes, solutions of the coupled-mode equations give rise to the anticrossing or Fano-resonance response. As clearly illustrated in Fig. 7, the anticrossing appears in the coupling between the magnetic resonance F and the chiral resonances G and H. The Fano resonance appears in the coupling between the chiral resonance I and magnetic resonances F, which is found in the S_{12} spectrum of Fig. 12. This difference in the coupling feature is elucidated by the field distributions of the chiral resonances. As discussed in the eigenmode analysis in Fig. 10, the chiral resonance I excludes the incident electric field from the metamolecule. This feature results in the weak coupling between the two resonance modes. On the other hand, the chiral resonances G and H do not exclude the incident electric field from the metamolecule, resulting in the strong coupling between the meta-atoms.

The giant MCh effect is traced back to the Fano resonance. Moreover, the gigantic feature originates from the strength difference between the Fano resonances of S_{12} and S_{21} as shown in Fig. 12. This difference is the result of the nonreciprocity of the interaction between the meta-atoms [38]. The chiral resonance is reciprocal. The chiral meta-atom is therefore on resonance when excited from either port. Whereas the magnetic meta-atom is also on resonance when excited from either port, the resonance has nonreciprocity such as Faraday rotation. Thus the interaction between the magnetic resonance F and chiral resonance I has nonreciprocity, resulting in the nonreciprocal coupling parameter K described

by $K(\rightarrow) \neq K(\leftarrow)$, where the arrows indicate the propagation direction of the incident microwave, $\vec{k}/|\vec{k}|$.

The coupling parameter when excited from port 2 results in strong Fano resonance, whereas that from port 1 results in quite weak resonance. This nonreciprocity in the resonance leads to the large amplitude difference. In other words, the metamolecule strongly absorbs the incident microwaves when excited from port 2, whereas it is almost transparent to the incident microwaves when excited from port 1. Namely, one-way transparency is realized in the MCh metamolecule. Very similar phenomena have been reported in natural materials at low temperature and/or under very strong magnetic field: in chiral-lattice magnet Cu_2OSeO_3 for microwaves [39,40] and multiferroic CuB_2O_4 for near-infrared light [23]. In the multiferroic materials, the one-way transparency is traced back to the interference between the $E1$ and $M1$ transitions under the condition that the two transitions have the same amplitude. Similarly, the interaction between the magnetic resonance F and chiral resonance I gives rise to the one-way transparency in the MCh metamolecule. Following the large amplitude difference caused by the one-way transparency, the phase difference between S_{21} and S_{12} becomes larger due to the Kramers-Kronig relation. We conclude that the giant MCh effect observed in the present study originates from the one-way transparency caused by the Fano resonance in the metamolecule.

V. CONCLUSIONS

In conclusion, we have experimentally and numerically studied enhanced MCh effects at microwave frequencies by a single metamolecule. Microwave transmission coefficients S_{21} and S_{12} through a single metamolecule consisting of a copper chiral structure and ferrite cylinder were measured under $\mu_0 H_{\text{ext}}$ up to ± 400 mT. By applying $\mu_0 H_{\text{ext}}$, the difference between S_{21} and S_{12} was observed in amplitude and phase, which was caused by the artificial MCh effect with simultaneous space-inversion and time-reversal symmetry breaking. As $\mu_0 H_{\text{ext}}$ was increased, the MCh signal associated with the magnetic resonance was shifted to a higher frequency and enhanced under strong $\mu_0 H_{\text{ext}}$. In contrast, the MCh signals associated with the chiral resonances shifted slightly to higher frequencies and became large as the magnetic resonance approached, while the signals jumped to lower frequencies flipping sign after passed by the magnetic resonance. The nonreciprocal differences in the real and imaginary parts of refractive indices due to the enhanced MCh effects observed in the experiments were increased up to $\Delta n' \simeq -8.9 \times 10^{-2}$ and $\Delta n'' \simeq -2.6 \times 10^{-1}$ maxima by applying $\mu_0 H_{\text{ext}} = +400$ mT.

The experimental results were reproduced well by numerical calculation using a finite element method. Notably, we predicted in the numerical calculation that the MCh effect was significantly enhanced to $\Delta n' \simeq -6.6 \times 10^{-1}$ and $\Delta n'' \simeq -1.26$ maxima by interacting the magnetic resonance with the "exclusive" chiral resonance at a higher frequency. The mechanism of the giant MCh effect was revealed by investigating eigenmodes and electromagnetic field distributions in the metamolecule. Nonreciprocal Fano resonance between the magnetic resonance and exclusive chiral resonance in the meta-atoms is a key in the giant MCh effects. As a consequence of the nonreciprocal Fano resonance, one-way transparency is realized in the MCh metamolecule at room temperature and convenient magnetic field strength. These conditions are quite preferable for practical applications such as a one-way mirror. The present study enables us to obtain large directional birefringence, opening the door toward the realization of a synthetic gauge field, for example, an effective magnetic field for electromagnetic waves [9,10], and toward *meta-condensed-matter physics* using metamaterials.

ACKNOWLEDGMENTS

The authors acknowledge Andrey Porokhnyuk, Leigh McDowell, Tomomi Suwa, and Nobuyoshi Hosoito for valuable discussion. We also acknowledge Masanobu Iwanaga and Hideki T. Miyazaki of NIMS. Financial support of this work by JSPS KAKENHI (Grants No. 25889001 and No. 26287065) is also acknowledged.

[1] F. Englert and R. Brout, Phys. Rev. Lett. **13**, 321 (1964).
[2] P. W. Higgs, Phys. Rev. Lett. **13**, 508 (1964).
[3] H. E. Stanley, *Introduction to Phase Transitions and Critical Phenomena* (Oxford University Press, New York, 1988).
[4] E. Hecht, *Optics* (Pearson Education Limited, Harlow, 2013).
[5] N. B. Baranova, Yu. V. Bogdanov, and B. Ya. Zel'dovich, Opt. Commun. **22**, 243 (1977).
[6] G. Wagnière and M. Meier, Chem. Phys. Lett. **93**, 78 (1982).
[7] L. D. Barron and J. Vrbancich, Mol. Phys. **51**, 715 (1984).
[8] G. L. J. A. Rikken and E. Raupach, Nature (London) **390**, 493 (1997).
[9] K. Sawada and N. Nagaosa, Phys. Rev. Lett. **95**, 237402 (2005).
[10] K. Fang, Z. Yu, and S. Fan, Nat. Photonics **6**, 782 (2012).
[11] S. Mühlbauer, B. Binz, F. Jonietz, C. Pfleiderer, A. Rosch, A. Neubauer, R. Georgii, and P. Böni, Science **323**, 915 (2009).
[12] G. L. J. A. Rikken and E. Raupach, Phys. Rev. E **58**, 5081 (1998).
[13] P. Kleindienst and G. H. Wagnière, Chem. Phys. Lett. **288**, 89 (1998).
[14] M. Vallet, R. Ghosh, A. Le Floch, T. Ruchon, F. Bretenaker, and J.-Y. Thépot, Phys. Rev. Lett. **87**, 183003 (2001).
[15] V. Krstić, S. Roth, M. Burghard, K. Kern, and G. L. J. A. Rikken, J. Chem. Phys. **117**, 11315 (2002).
[16] V. A. Sautenkov, Y. V. Rostovtsev, H. Chen, P. Hsu, Girish S. Agarwal, and M. O. Scully, Phys. Rev. Lett. **94**, 233601 (2005).
[17] M. Saito, K. Ishikawa, K. Taniguchi, and T. Arima, Phys. Rev. Lett. **101**, 117402 (2008).
[18] S. Bordàcs, I. Kézsmárki, D. Szaller, L. Demkó, N. Kida, H. Murakawa, Y. Onose, R. Shimano, T. Rõõm, U. Nagel, S. Miyahara, N. Furukawa, and Y. Tokura, Nat. Phys. **8**, 734 (2012).
[19] S. Kibayashi, Y. Takahashi, S. Seki, and Y. Tokura, Nat. Commun. **5**, 4583 (2014).

[20] M. Saito, K. Taniguchi, and T. Arima, J. Phys. Soc. Jpn. **77**, 013705 (2008).
[21] I. Kézsmárki, N. Kida, H. Murakawa, S. Bordàcs, Y. Onose, and Y. Tokura, Phys. Rev. Lett. **106**, 057403 (2011).
[22] I. Kézsmárki, D. Szaller, S. Bordács, V. Kocsis, Y. Tokunaga, Y. Taguchi, H. Murakawa, Y. Tokura, H. Engelkamp, T. Rõõm, and U. Nagel, Nat. Commun. **5**, 3203 (2014).
[23] S. Toyoda, N. Abe, S. Kimura, Y.-H. Matsuda, T. Nomura, A. Ikeda, S. Takeyama, and T. Arima, Phys. Rev. Lett. **115**, 267207 (2015).
[24] N. Kida, T. Yamada, M. Konoto, Y. Okimoto, T. Arima, K. Koike, H. Akoh, and Y. Tokura, Phys. Rev. Lett. **94**, 077205 (2005).
[25] N. Kida, Y. Kaneko, J. P. He, M. Matsubara, H. Sato, T. Arima, H. Akoh, and Y. Tokura, Phys. Rev. Lett. **96**, 167202 (2006).
[26] N. Kida, H. Yamada, H. Sato, T. Arima, M. Kawasaki, H. Akoh, and Y. Tokura, Phys. Rev. Lett. **99**, 197404 (2007).
[27] K. Sawada and N. Nagaosa, Appl. Phys. Lett. **87**, 042503 (2005).
[28] D. R. Smith, J. B. Pendry, and M. C. K. Wiltshire, Science **305**, 788 (2004).
[29] D. R. Smith, W. J. Padilla, D. C. Vier, S. C. Nemat-Nasser, and S. Schultz, Phys. Rev. Lett. **84**, 4184 (2000).
[30] J. B. Pendry, A. J. Holden, W. J. Stewart, and I. Youngs, Phys. Rev. Lett. **76**, 4773 (1996).
[31] J. B. Pendry, A. J. Holden, D. R. Robbins, and M. J. Stewart, IEEE Trans. Microwave Theory Tech. **47**, 2075 (1999).
[32] S. Tomita, K. Sawada, A. Porokhnyuk, and T. Ueda, Phys. Rev. Lett. **113**, 235501 (2014).
[33] *Electromagnetic Fields in Unconventional Materials and Structures*, edited by O. N. Singh and A. Lakhtakia (Wiley-Interscience, New York, 2004).
[34] K. F. Lindman, Ann. Phys. (NY) **368**, 621 (1920).
[35] D. M. Pozar, *Microwave Engineering*, 3rd ed. (Wiley, New York, 2004).
[36] G. B. G. Stenning, G. J. Bowden, L. C. Maple, S. A. Gregory, A. Sposito, R. W. Eason, N. I. Zheludev, and P. A. J. de Groot, Opt. Express **21**, 1456 (2013).
[37] B. Peng, Ş. K. Özdemir, W. Chen, F. Nori, and L. Yang, Nat. Commun. **5**, 5082 (2014).
[38] S. H. Mousavi, A. B. Khanikaev, J. Allen, M. Allen, and G. Shvets, Phys. Rev. Lett. **112**, 117402 (2014).
[39] Y. Okamura, F. Kagawa, S. Seki, M. Kubota, M. Kawasaki, and Y. Tokura, Phys. Rev. Lett. **114**, 197202 (2015).
[40] M. Mochizuki, Phys. Rev. Lett. **114**, 197203 (2015).